

A New Software Tool for Quantitative Verification of IMRT Fluence Maps

Introduction: A great deal of physics effort is currently spent on IMRT QA and on developing IMRT QA techniques and standards. The most common IMRT validation technique involves delivering a patient plan to a QA phantom. Most physicists would agree that this is currently considered the “gold standard” of IMRT QA. The dose distribution is calculated in the phantom by the treatment planning system, and measurements are then performed to check the point dose and/or the plane dose distribution against those predicted by treatment planning system (TPS). This technique is very time consuming and labor intensive. Moreover, other techniques exist which may be more sensitive to minor calculation or delivery errors than the aforementioned technique. For example, if a few bixels in one fluence map are in error by a significant amount, there is no guarantee that the phantom dosimetry technique will reveal this error. Secondary dose calculation algorithms are in widespread use to verify the accuracy of the dose calculation by the TPS, however, a verification of the delivery mechanism must accompany such software to assure appropriate QA for the entire IMRT process.

We developed a new software tool called Super-IMPOSE (Intensity Map Pre-treatment OverSight & Evaluation) to quantitatively verify 2-dimensional fluence maps using a flat-panel amorphous silicon Electronic Portal Imager (EPI). This software tool, written in C++, imports images of fluence maps delivered to the EPI along with fluence maps from the treatment planning system and compares them bixel by bixel. Since the EPI image includes the effects of scatter within the imager, we developed a convolution algorithm to create a scatter-corrected fluence map from the raw fluence map. The convolution kernel is based on measured data from the EPI. Once the maps and image data are imported into the software, an in-house algorithm is used to accurately detect the edges of the measured and intended fluence maps and register them to one another. Both maps are then normalized to the highest intensity bixel to create relative image maps. Finally, deviations between the predicted bixel values (after scatter-correction) and measured bixel values are calculated. The results are displayed as a matrix of percentage deviations for each bixel in the fluence map, with maximum, mean, and standard deviation values calculated for each row, each column, and the whole fluence map. Clinical applicability was investigated using IMRT plans generated using the Corvus treatment planning system and delivered using a Varian accelerator with an aS500 EPI. A set of 16 fluence maps taken from 6 different patients was selected, spanning a wide range of field sizes, using a wide range of EPI positions (104-160 cm SDD), and using both 5 mm x 5 mm and 1 cm x 1 cm bixel sizes.

Linearity of Dose Response of EPI: Greer^[i] and Cremers^[ii] investigated properties of EPIs for IMRT QA and compared them to ion chamber and film for open and wedged static fields and IMRT fields. Their results showed that the response of the EPID was linear with dose and dose rate. The agreement between the EPID profiles and ion chamber dosimetry and film dosimetry was within 5%.

Convolution Kernel: We generated a convolution scatter kernel for a Varian Clinac 2300EX linac equipped with a Varian Millennium-120 multi-leaf collimator (Varian Medical System, Palo Alto, CA) from experimental data. Figure (1) shows the experimental scatter distribution in 3x3 cm area.

Registration of Fluence Map and EPI: An advanced algorithm was developed to automatically detect the edge on both fluence map and EPI image. The registration correlates the fluence map with the EPI image, taking into account SSD, bixel size, and pixel size.

Clinical Application: The mean and standard deviation of the bixel intensity differences were 2.55% and 1.57%. As one would expect, these values were significantly better for the 1 cm bixel size (1.94% and 1.36%, respectively) than for the 5 mm bixel size (3.16% and 1.79%, respectively). The largest deviation observed for all bixels in all maps was 14.3%. These differences are, in general, quite small with respect to the intensity step size of 10% used for modulation of these beams. It is therefore easy to be assured that the correct intensity level was delivered to the vast majority of bixels. Use of the scatter correction algorithm reduced bixel differences by an average of 300% compared with uncorrected fluence maps. It is expected that the smaller bixel size will result in larger differences. Some reasons may include: (1) smaller bixels result in more complex scatter distributions to adjacent bixels; (2) the residual error is larger for a smaller bixel during the conversion from an integer number to a float in the image registration mechanism. Therefore, small errors in the convolution kernel will be magnified. Figure (2) shows a typical QA result for a patient study. Figure (3) shows an EPI image next to the intended fluence map after scatter correction.

Conclusion: EPI-based QA using our software tool provides a relatively accurate and very expeditious means for performing IMRT delivery QA, allowing verification of all maps in a matter of minutes. The development of a more accurate convolution kernel will allow us to reduce our uncertainties in comparison of delivered to intended fluence maps. In the near future, we plan to artificially introduce errors into the fluence maps and determine whether phantom QA or the technique described here is more sensitive in detecting these errors.

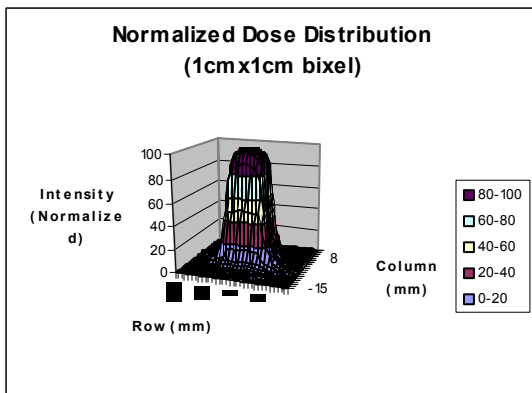


Figure (1)

Study: 2285 Port: Couch 0 , Gantry 0

R/C	1	2	3	4	5	6	7	8	9	10	Max	Mean	STD
1	0.347	0.509	3.573	3.466	0.874	0.924	0.036	0.105	0.094	0.000	3.573	0.993	0.996
2	1.976	1.129	1.786	3.726	2.011	0.751	1.027	0.730	0.543	0.094	3.726	1.377	1.174
3	1.521	0.593	3.049	3.730	5.303	4.738	2.620	1.090	1.330	0.236	5.303	2.421	1.556
4	3.808	1.622	0.970	0.608	0.439	0.599	1.356	0.270	0.032	2.514	3.808	1.222	1.105
5	0.310	3.460	2.929	2.704	2.894	2.433	1.375	2.546	3.296	0.055	3.460	2.200	1.483
6	1.035	1.429	0.653	0.375	0.064	0.072	0.306	2.515	2.835	1.083	2.835	1.037	1.018
7	0.418	1.755	1.063	0.579	0.031	0.037	0.432	1.952	3.498	3.280	3.498	1.304	1.142
8	3.581	1.721	0.773	1.123	1.229	0.034	0.361	1.036	2.025	0.636	3.581	1.252	1.119
9	2.028	0.155	0.191	0.643	3.930	5.983	1.878	1.259	0.280	6.043	6.043	2.239	1.496
10	0.143	2.388	2.475	1.030	0.953	0.018	5.587	3.942	5.805	0.852	5.805	2.319	1.523
Max	3.808	3.460	3.573	3.730	5.303	5.983	5.587	3.942	5.805	6.043	0.000	0.000	0.000
Mean	1.517	1.476	1.746	1.798	1.773	1.559	1.498	1.545	1.974	1.479	0.000	0.000	0.000
STD	1.232	1.215	1.321	1.341	1.331	1.249	1.224	1.243	1.405	1.216	0.000	0.000	0.000

Whole Map: Max = 6.043, Mean = 1.636, STD = 1.279

Figure (2)

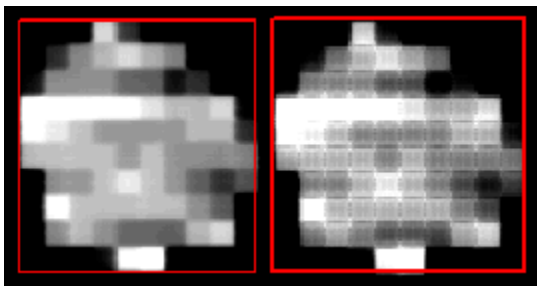


Figure (3)

ⁱ Greer PB, Popescu CC. Dosimetric properties of an amorphous silicon electronic portal imaging device for verification of dynamic intensity modulated radiation therapy. *Med Phys* 2003; 30:1618-1627.

ⁱⁱ Cremers F, Frenzel T, Kausch C, Albers D, Schonborn T, Schmidt R. Performance of electronic portal imaging devices (EPIDs) used in radiotherapy: image quality and dose measurements. *Med Phys* 2004; 31:985-996.